Flexible tuning of nonlinear non-diffracting array beams using wavelengths and angles

Dongmei Liu,[1,2] **Yong Zhang,**[3,4] ID **Xiaopeng Hu,**[3] ID **Peng Han,**[1] **Min Gu,**[1,*] **and Min Xiao**[2,3]

[1]*School of Physics and Telecommunication Engineering, South China Normal University, Guangzhou 510006, China*
[2]*Department of Physics, University of Arkansas, Fayetteville, Arkansas 72701, USA*
[3]*National Laboratory of Solid State Microstructures, Nanjing University, Nanjing 210093, China*
[4]*e-mail:zhangyong@nju.edu.cn*
Corresponding author: mingu@m.scnu.edu.cn

We present a simple method to enable flexible tuning of non-diffracting beams in a two-dimensional nonlinear photonic crystal, based on the interference of two or more non-collinear second-harmonic beams. By manipulating the wavelengths of the beams and the angle of incidence of the fundamental wave, the arbitrary period and propagation length, as well as the wavelength of the generated nonlinear non-diffracting array beams, can be tuned flexibly. These light beams can trap and manipulate multiple particles, create new forms of optical imaging systems, and act within nonlinear devices to bring novel functionalities to integrated optics. © 2020 Optical Society of America

https://doi.org/10.1364/OL.402876

The non-diffracting beam, i.e., a solution to the Helmholtz equation, has a transverse intensity distribution that is independent of its propagation distance. So far, there are two major types of non-diffracting beams, Airy and Bessel beams, which are extensively studied. The Bessel beam was first reported by Durnin *et al.* in 1987, when they illuminated a circular slit located within the focal plane of a lens [1]. Due to its peculiar properties, the Bessel beams have found a variety of applications ranging from medical cell imaging [2], particle trapping [3], optical micromanipulation [4], to microscopy [5]. The extension to terahertz (THz)-level Bessel beams through the use of a quarter-wave plate and Teflon axicon is particularly useful [6], owing to the lack of efficient optics available for this wavelength range. Additionally, experimental verification of the electron Bessel beam has gained the intriguing performance [7]. Recent progress on traditional Bessel beams has been made with axicons [8,9], multimode optical fibers [10], metasurfaces [11], and optical coherence lattices [12]. Generating an ideal Bessel beam is impossible because it carries infinite energy. A couple of other different methods with better efficiency, such as surface plasmon polaritons (SPPs) and nonlinear photonic crystals (NPCs), were proposed and demonstrated experimentally to generate cosine beams [13–15].

Benefited from the development of the two-dimensional (2D) NPC [16], numerous optical effects have been discovered. Recently, we reported a novel tunable non-diffracting array beam in periodically poled LiTaO$_3$ crystals, wherein non-diffracting beams are formed by the generation of second-harmonic (SH) waves [15]. The prerequisite to realize the non-diffracting array beams is the satisfaction of the non-collinear quasi-phase-matching (QPM) condition. These observations also offer a flexible way to generate tunable non-diffracting array beams in nonlinear crystals without changing the involved devices. Although a theoretical description was developed to interpret the observed non-diffracting array, the focus was mainly on non-diffracting array beams under the QPM condition at normal incidence [15]. Therefore, further studies are necessary for the non-diffracting beams under non-QPM (i.e., the pump wavelength slightly away from the perfect QPM wavelength, the additional vector is not exactly compensating the phase mismatch.) conditions both at normal incidence and oblique incidence.

In this paper, we experimentally demonstrate flexible control of nonlinear non-diffracting array beams by varying the pump wavelengths and incident angles in a 2D NPC. As illustrated in Fig. 1(a), the NPC has a squarely poled structure with a period of $\Lambda = 5.5$ μm and a duty cycle of ∼35%. The pump beam is directed into the NPC at an angle θ along the y axis of the crystal. The QPM diagram exhibited in Fig. 1(b) combines the wave vectors k_1 and k_2 (or k'_2), which correspond to the beam's fundamental frequency and its SH, respectively. According to the SH conversion efficiency, the incident angle θ is very small. By using the reciprocal vectors $G_{m,-i}$ and $G_{m,j}$, non-collinear QPM SH generation (SHG) can be realized at the oblique incidence, where m, i, and j are the nonlinear diffraction orders.

The theoretical investigation is similar to that presented in Ref. [15], here we produce a flexible tuning non-diffracting array through a SHG process in a 2D NPC as shown in Fig. 1(a). The coupled-wave equations are given by

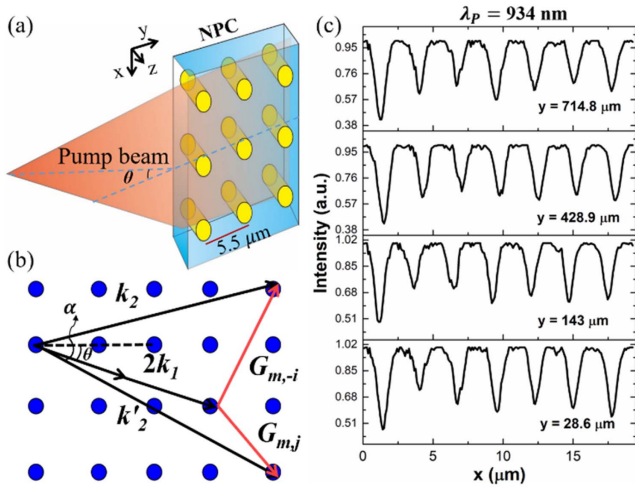$$\nabla^2 E_2 + k_2^2 E_2 = \frac{1}{2} K t(x, y) E_1^2, \tag{1}$$

Fig. 1. (a) Illustration of nonlinear non-diffracting array beam generation. (b) Non-collinear QPM diagram. (c) Non-diffracting SH array beam at certain observation planes is obtained at the $\lambda_P = 934$ nm.

$$\nabla^2 E_2' + k_2'^2 E_2' = \frac{1}{2} K t(x, y) E_1^2, \tag{2}$$

where E_1 and E_2 (or E_2') are the electrical fields of the fundamental wave and SH wave, respectively. k_2 and k_2' represent the wave vectors of the SH wave in two SHG processes, which involve different reciprocal vectors. In Eqs. (1) and (2), K is the coupling coefficient, and it is determined by the second-order susceptibility $\chi^{(2)}$, while $t(x, y)$ is the structural function of the NPC. We seek a non-diffracting solution for the SH waves, which are given by

$$E_2(x, y) = A \exp(i k_{2y} y) \cos(k_{2x} x), \tag{3}$$

$$E_2'(x, y) = A' \exp(i k_{2y}' y) \cos(k_{2x}' x). \tag{4}$$

The quantities A and A' are constant, and $k_{2x} (k_{2x}')$ and $k_{2y} (k_{2y}')$ are, respectively, the x and y components of the SH wave vectors. The electrical field distribution along z direction is uniform in this case. The cosine beams described by Eqs. (3) and (4) can be considered as two plane wave components and thus give rise to the non-diffracting solution. Obviously, such solution has a transverse intensity profile independent of the propagation direction y, which represents a non-diffracting SH array.

The QPM conditions under non-collinear configuration [Fig. 1(b)] at the oblique incidence require

$$\vec{k_2} - 2\vec{k_1} - \vec{G_{m,-i}} = 0, \tag{5}$$

$$\vec{k_2'} - 2\vec{k_1} - \vec{G_{m,j}} = 0. \tag{6}$$

Interestingly, the reciprocal vectors $G_{m,-i}$ and $G_{m,j}$ can simultaneously generate two asymmetric SH waves as shown in Fig. 1(b), which can be considered as the decomposed components of the cosine beam in Eqs. (3) and (4). They interfere with each other and result in a non-diffracting SH array, which is similar to that reported in Ref. [15]. Considering that the two SH components of the cosine beam have an in-between angle of

α [decided by Eqs. (5) and (6)] in Fig. 1(b), the transverse profile of the SH intensity can be easily deduced to be

$$I_{SH}(x) \propto \cos\left(\frac{2\pi i}{\Lambda} x\right) \cos\left(\frac{2\pi j}{\Lambda} x\right). \tag{7}$$

The generated SH waves interfere with each other and, therefore, produce nonlinear non-diffracting array beams. After some algebra, the period of the array Λ' is obtained as

$$\Lambda' = \Lambda/(i + j), \tag{8}$$

where Λ is the period of NPC, and i and j are the dominant diffraction orders. Here $i = j$ corresponds to normal incidence, whereas $i \neq j$ denotes the oblique incidence. The propagation length of the SH array beam is determined by $L = d/\sin \alpha$, where d is the diameter of the input laser. Unlike the other non-diffracting beam schemes, in which the periods and propagation lengths are usually fixed by a sample structure or the device used, here a given NPC can generate non-diffracting array beams with varied periods and propagation lengths using different reciprocal vectors $G_{m,-i}$ and $G_{m,j}$ [see Fig. 1(b)]. The different vectors can be selected by simply varying the incident angle or tuning the fundamental wavelength. In our scheme, the prerequisite for the realization of the non-diffracting array beams is the non-collinear SH beams, regardless of whether they completely satisfy the QPM condition or not. The generated SH waves then interfere with one another to produce the non-diffracting array beams.

By the aid of the above theoretical study, we perform experimental measurement of the non-diffracting array beam. In the current configuration, the working wavelength of pump laser is tuned from 900 nm to 960 nm, and the generated SH wave has a wavelength from 450 nm to 480 nm. The incident light power is kept at 60 mW for all the wavelengths. The SHG efficiency is about 4.7%. In our previous work [15], a NPC was placed approximately perpendicular to the light propagation direction. To manipulate the sample accurately, the NPC was fixed using a rotating stage in the experiment. Similar to our previous studies on QPM diffraction-free array beam [15], a charge-coupled device (CCD) camera is used to record the SH patterns. The pump laser is first set to 934 nm under the normal incidence, and the generated SH wave is 467 nm. As indicated in Fig. 1(c), the measured SH array beams at certain observation planes clearly exhibit the non-diffracting performance. Although the intensity of the SH beams slightly reduces, the period of the array does not change from $y = 28.6$ μm to $y = 714.8$ μm. In our experiment, the non-diffracting SH beam can be observed at a distance of up to 1.7 mm away from the NPC with a pump wavelength of 934 nm.

Besides, we observed the near-field characteristic of non-diffracting array beams at normal incidence, wherein the generated non-collinear SH beams are always symmetrical. The characteristic SH beams that were recorded at different input wavelengths at the output face of the NPC are shown on the left of Fig. 2. To further examine the observed SH patterns, we have chosen a cross section, which is marked with the red double arrow at the same location in all the patterns in Fig. 2, to present period change with wavelength as shown in Fig. 3. As indicated in Figs. 2(a)–2(c), the diffraction patterns change considerably when the wavelength was increased. For example, when the input laser was set to be 909 nm [Fig. 2(a)], the period
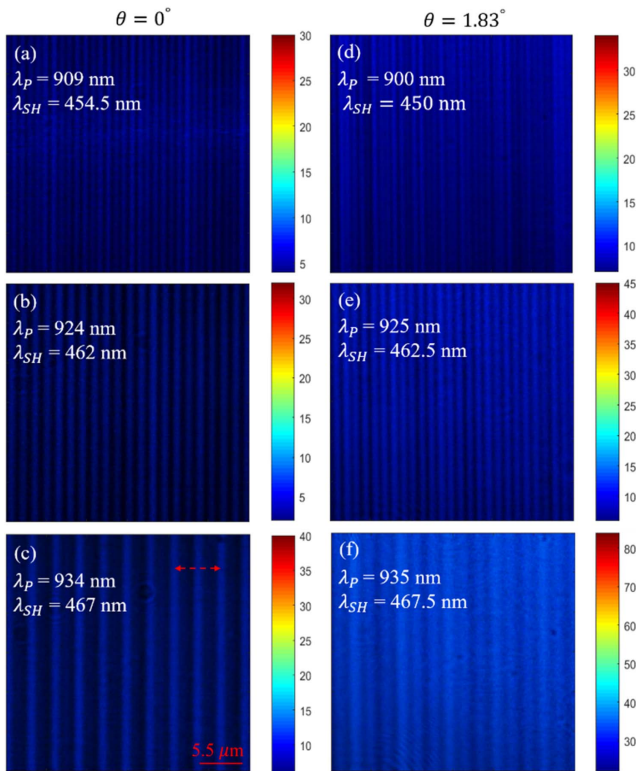
Fig. 2. Measured characteristic cross sections of the non-diffracting array beams at the output face of the NPC for different input wavelengths. (a)–(c) Normal incidence and (d)–(f) oblique incidence at an angle of $\theta = 1.83°$. The red double arrow in (c) denotes the cross section in all the images in Fig. 2, wherein we measure the period change with the input wavelength as shown in Fig. 3.

Fig. 3. Changes between the period and the input wavelength under two input angles. (a) The measured periods of the arrays are 0.928 μm, 1.39 μm, and 2.78 μm at pump wavelengths of 909 nm, 924 nm, and 934 nm under $\theta = 0°$, respectively. (b) The periods of the arrays are 0.80 μm, 1.11 μm, and 1.86 μm at the pump wavelengths of 900 nm, 925 nm, and 935 nm under $\theta = 1.83°$, respectively.

of the generated SH array is 0.928 μm [as indicated by the blue line in Fig. 3(a)]. It is almost the same period as that at 906 nm (0.92 μm), which satisfies the perfect QPM condition [15]. So we can find that the reciprocal vectors $G_{1,3}$ and $G_{1,-3}$ played a key role in the generation of SH array beam at $\lambda_P = 909$ nm. According to the Eq. (8), the theoretical period of the SH image is $\Lambda' = \frac{5.5 \, \mu m}{3+3} = 0.917$ μm, which is consistent with the experimental data. We vary the pump wavelength to 924 nm and 934 nm. Compared with the pattern in Fig. 2(a), the SH array beams change dramatically as shown in Figs. 2(b) and 2(c). The period of the SH pattern at $\lambda_P = 924$ nm is 1.39 μm, as indicated by the red line in Fig. 3(a), which represents 1/4 of the domain period. It should be noted that the intensity of the stripes in Fig. 2(b) is almost uniform. When the pump wavelength is 934 nm [Fig. 2(c)], the SH array period becomes 2.78 μm, which is approximately 1/2 of the sample period as shown in Fig. 3(a) with a black line. Note that the SH patterns at $\lambda_P = 924$ nm and $\lambda_P = 934$ nm, respectively, have the same period with those reported at wavelengths of 928 and 944 nm under the QPM condition [15]. For these slightly away from QPM wavelengths, we can deduce that the reciprocal vectors, which play the major role in generation of non-diffracting SH array beam, are $G_{1,2}/G_{1,-2}$ and $G_{1,1}/G_{1,-1}$ at wavelengths of 924 nm and 934 nm, respectively. So the non-diffracting SH array beams could still be observed at these pump wavelengths. Different from the QPM case, the generated non-diffracting SH array beams have lower intensity in our experiment. We
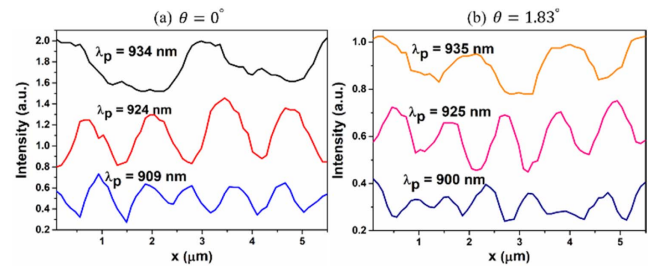
notice that the wavelength can be tuned about 10 nanometers away from the QPM resonance when the lower-order reciprocal vectors are involved to generate non-diffracting array beams, in contrary, only a few nanometers away from the perfect QPM wavelength with the higher-order reciprocal vectors under the normal incidence.

Then, we check the non-diffracting SH array beam at an oblique incidence (on the right of Fig. 2), i.e., the input angle $\theta = 1.83°$. We also analyzed the period change of the SH patterns at different wavelengths [Figs. 2(d)–2(f)]. In comparison with the $\theta = 0°$, the SH patterns also exhibit periodic arrays but with different periods and intensity at the $\theta = 1.83°$, as shown in Figs. 2(d)–2(f). At $\lambda_P = 900$ nm in Fig. 2(d), the array period reduces to 1/7 of the sample period, i.e., 0.8 μm [as indicated by the navy line in Fig. 3(b)] in the experiment, and the SH wavelength is 450 nm. Compared with Fig. 2(a), the SH array shown in Fig. 2(d) is not completely uniform, owing to the asymmetry SH waves that interfere to form the array beam. Then the pump wavelength was altered to 925 nm and 935 nm. As shown in Figs. 2(e) and 2(f), the SH beams change remarkably compared with the pattern excited by $\lambda_P = 900$ nm [Fig. 2(d)]. The period of the SH pattern at $\lambda_P = 925$ nm is 1.11 μm [Fig. 2(e) and pink line in Fig. 3(b)], which is 1/5 of the domain period. When λ_P further increases to 935 nm, the period becomes 1.86 μm [Fig. 2(f) and orange line in Fig. 3(b)], which corresponds to 1/3 of the sample period. The dependence of the period of non-diffracting SH array beams on the operating wavelength stems from the use of different reciprocal vectors, which will be discussed in detail in the next section.

We also measured the far-field SH patterns of different wavelengths at two input angles, where these patterns were projected onto a screen and recorded using a CCD camera. Figure 4 shows the vector diagram and the far-field SH beams at different pump wavelengths. As expected, the SH beams are arranged symmetrically, and the intensity is uniform under normal incidence. In contrast, under oblique incidence, the SH spots with non-uniform intensity are no longer symmetrical. Higher-order reciprocal vectors [e.g., $G_{1,3}/G_{1,-3}$ in Fig. 4(b) at $\lambda_P = 909$ nm and $G_{1,4}/G_{1,-3}$ in Fig. 4(c) at $\lambda_P = 900$ nm] emit far-field SH beams at a large α angle, which result in a non-diffracting array beam with a small period, as shown in Figs. 2(a) and 2(d). The SH array beams also have a low intensity, which agrees well with the near-field profiles shown in Figs. 3(a) and 3(b) (blue line and navy line). Interestingly, the far-field SH
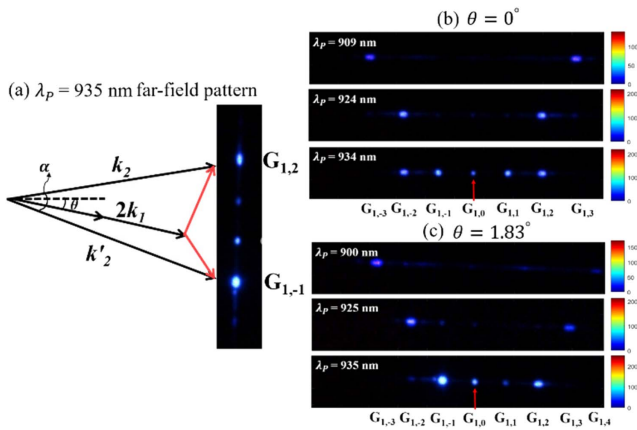
Fig. 4. Far-field SH beams decomposed from the non-diffracting beams at different input wavelengths. (a) The vector diagram to show the far-field image; far-field patterns under (b) normal incidence and (c) oblique incidence.

patterns change dramatically at pump wavelengths of 934 nm and 935 nm under different input angles, although these wavelengths are very close to each other. As indicated in Fig. 4(b), five SH spots are observed at 934 nm, which correspond to one collinear SH beam ($G_{1,0}$) and two pairs of symmetrical non-collinear SH beams ($G_{1,1}/G_{1,-1}$ and $G_{1,2}/G_{1,-2}$). Among these five spots, the second and fourth spots show the strongest intensity, which correspond to the reciprocal vectors $G_{1,1}$ and $G_{1,-1}$, respectively. Therefore, they interfere with each other to determine the period of SH pattern shown in Fig. 2(c). And the other spots ($G_{1,0}$ and $G_{1,2}/G_{1,-2}$) with the lower intensity interfere with one another to enhance the non-diffracting beam. According to the Eq. (8), the theoretical period of an array beam is $\Lambda' = \frac{5.5\,\mu m}{1+1} = 2.75\,\mu m$, which agrees well with the experimental result of 2.78 μm. However, there are only four SH spots at 935 nm as shown in Fig. 4(a) under the oblique incidence, where these spots from the top to bottom correspond to the reciprocal vectors $G_{1,2}$, $G_{1,1}$, $G_{1,0}$, and $G_{1,-1}$. Since the SH beams $G_{1,2}$ and $G_{1,-1}$ have larger intensity, they play the dominant role in the generation of non-diffracting array beams at $\lambda_P = 935$ nm. The theoretical period of the SH image at 935 nm is 1.83 μm, which is in good agreement with our experimental data 1.86 μm [shown in Fig. 2(f)]. Obviously, the intensity of the collinear SH beam $G_{1,0}$ [indicated by the red arrows in Figs. 4(b) and 4(c)] is very low, which makes almost no contribution to the generation of non-diffracting array beams. In addition, the non-collinear SH beams $G_{1,2}$ and $G_{1,-2}$ [at $\lambda_P = 924$ nm in Fig. 4(b)] interfere with each other to form the pattern shown in Fig. 2(b), and the asymmetrical SH beams $G_{1,-2}/G_{1,3}$ [$\lambda_P = 925$ nm in Fig. 4 (c)] participate in the formation of the image presented in Fig. 2(e). Based on these observations, the non-diffracting array beams are indeed generated by the interference of non-collinear SH beams in our configuration.

As mentioned above, our method can be regarded as the interference of the non-collinear SH beams, which is similar to the previously reported methods that are applied an axicon [9] or SPPs [13,14]. In the nonlinear crystal, the exit angle of the non-collinear SH beam could be flexibly tuned by varying the pump wavelength and incident angle. The method, therefore, involves

different reciprocal vectors, which is the key factor for the realization of tunable non-diffracting array beams. Additionally, we notice that the generation of non-diffracting SH beams is more efficient under QPM condition, and it has a good tolerance on the pump wavelength or angular tuning. This feature was not confirmed in our previous work [15]. It should also be noted that although all the SH beams are involved in the formation of the non-diffracting array, only the two major non-collinear beams, which have stronger intensity, play a decisive role in the process. Similar to the 935 nm, the SH beams $G_{1,-1}$ and $G_{1,2}$ are predominant, and the collinear SH beam hardly makes any contribution to the non-diffracting array beam. Therefore, the collinear QPM could be avoided or a blocker could be used to remove the collinear SH beam, which would allow better images to be realized.

In summary, we have presented a method for flexible control of non-diffracting SH array beams by tuning the pump wavelengths and incident angles in a 2D NPC. In particular, our experiments indicate that the non-QPM SHG process must be taken into account, when analyzing the details of the non-diffracting beams under different conditions, as is the case with the QPM SHG process. By including these two factors, the generated non-diffracting array beams could be flexibly tuned including their period, propagation distance, and wavelength in a fixed nonlinear crystal.

Disclosures. The authors declare no conflicts of interest.

REFERENCES

1. J. Durnin, J. Miceli, Jr., and J. H. Eberly, Phys. Rev. Lett. **58**, 1499 (1987).
2. L. Gao, L. Shao, B. C. Chen, and E. Betzig, Nat. Protoc. **9**, 1083 (2014).
3. G. Milne, K. Dholakia, D. McGloin, K. Volke-Sepulveda, and P. Zemanek, Opt. Express **15**, 13972 (2007).
4. Y. A. Ayala, A. V. Arzola, and K. Volke-Sepulveda, Opt. Lett. **41**, 614 (2016).
5. F. O. Fahrbach, P. Simon, and A. Rohrbach, Nat. Photonics **4**, 780 (2010).
6. Z. Wu, X. Wang, W. Sun, S. Feng, P. Han, J. Ye, and Y. Zhang, Sci. Rep. **7**, 13929 (2017).
7. V. Grillo, E. Karimi, G. C. Gazzadi, S. Frabboni, M. R. Dennis, and R. W. Boyd, Phys. Rev. X **4**, 011013 (2014).
8. G. Antonacci, D. Caprini, and G. Ruocco, Appl. Phys. Lett. **114**, 013502 (2019).
9. N. Mahmood, H. Jeong, I. Kim, M. Q. Mehmood, M. Zubair, A. Akbar, M. Saleem, M. S. Anwar, F. A. Tahir, and J. Rho, Nanoscale **11**, 20571 (2019).
10. X. Zhu, A. Schulzgen, L. Li, and N. Peyghambarian, Appl. Phys. Lett. **94**, 201102 (2009).
11. W. T. Chen, M. Khorasaninejad, A. Y. Zhu, J. Oh, R. C. Devlin, A. Zaidi, and F. Capasso, Light Sci. Appl. **6**, e16259 (2017).
12. C. Liang, X. Zhu, C. Mi, X. Peng, F. Wang, Y. Cai, and S. A. Ponomarenko, Opt. Lett. **43**, 3188 (2018).
13. J. Lin, J. Dellinger, P. Genevet, B. Cluzel, F. de Fornel, and F. Capasso, Phys. Rev. Lett. **109**, 093904 (2012).
14. E. Megidish, A. Halevy, H. S. Eisenberg, A. Ganany-Padowicz, N. Habshoosh, and A. Arie, Opt. Express **21**, 6689 (2013).
15. D. Liu, D. Wei, Y. Zhang, Z. Chen, R. Ni, B. Yang, X. Hu, Y. Q. Qin, S. N. Zhu, and M. Xiao, Sci. Rep. **7**, 40856 (2017).
16. I. Epstein, R. Remez, Y. Tsur, and A. Arie, Optica **3**, 15 (2016).